CHEMISTRY OF MATERIALS

Subscriber access provided by Kaohsiung Medical University

Article

Low-Temperature Tailoring of Copper-Deficient Cu^{3-x}P – Electric Properties, Phase Transitions and Performance in Lithium-Ion Batteries

Alexander Wolff, Thomas Doert, Jens Hunger, Martin Kaiser, Julia Pallmann, Romy Reinhold,
Sivatmeehan Yogendra, Lars Giebeler, Jörg Sichelschmidt, Walter Schnelle, Rachel Whiteside,
H. Q. Nimal Gunaratne, Peter Nockemann, Jan J. Weigand, Eike Brunner, and Michael Ruck

Chem. Mater., **Just Accepted Manuscript** • DOI: 10.1021/acs.chemmater.8b02950 • Publication Date (Web): 17 Sep 2018

Downloaded from http://pubs.acs.org on September 18, 2018

Just Accepted

“Just Accepted” manuscripts have been peer-reviewed and accepted for publication. They are posted online prior to technical editing, formatting for publication and author proofing. The American Chemical Society provides “Just Accepted” as a service to the research community to expedite the dissemination of scientific material as soon as possible after acceptance. “Just Accepted” manuscripts appear in full in PDF format accompanied by an HTML abstract. “Just Accepted” manuscripts have been fully peer reviewed, but should not be considered the official version of record. They are citable by the Digital Object Identifier (DOI®). “Just Accepted” is an optional service offered to authors. Therefore, the “Just Accepted” Web site may not include all articles that will be published in the journal. After a manuscript is technically edited and formatted, it will be removed from the “Just Accepted” Web site and published as an ASAP article. Note that technical editing may introduce minor changes to the manuscript text and/or graphics which could affect content, and all legal disclaimers and ethical guidelines that apply to the journal pertain. ACS cannot be held responsible for errors or consequences arising from the use of information contained in these “Just Accepted” manuscripts.

ACS Publications

is published by the American Chemical Society. 1155 Sixteenth Street N.W., Washington, DC 20036

Published by American Chemical Society. Copyright © American Chemical Society. However, no copyright claim is made to original U.S. Government works, or works produced by employees of any Commonwealth realm Crown government in the course of their duties.

Low-Temperature Tailoring of Copper-Deficient Cu$_{3-x}$P – Electric Properties, Phase Transitions and Performance in Lithium-Ion Batteries

Alexander Wolff,[†] Thomas Doert,[†] Jens Hunger,[†] Martin Kaiser,[†] Julia Pallmann,[†] Romy Reinhold,[‡] Sivatmeehan Yogendra,[†] Lars Giebeler,[‡] Jörg Sichelschmidt,[‖] Walter Schnelle,[‖] Rachel Whiteside,[#] H. Q . Nimal Gunaratne,[#] Peter Nockemann,[#] Jan J. Weigand,[†] Eike Brunner[†] and Michael Ruck*[,†,‖]

[†] Faculty of Chemistry and Food Chemistry, Technische Universität Dresden, 01062 Dresden, Germany.

[‡] Leibniz Institute for Solid State and Material Research Dresden e. V., 01069 Dresden, Germany.

[‖] Max Planck Institute for Chemical Physics of Solids, 01187 Dresden, Germany.

[#] School of Chemistry and Chemical Engineering, Queen's University of Belfast, Belfast BT71NN, United Kingdom.

ABSTRACT: A convenient approach for a controlled and high-yield synthesis of copper-deficient Cu$_{3-x}$P $(0.1 < x < 0.7)$ is reported that makes use of ionic liquids with highly nucleophilic "naked" halide anions. Halide anions drastically enhance the reactivity of the white phosphorus precursor and kinetically disfavour the formation of phosphorus-rich side products. Cu$_{3-x}$P shows a high degree of tolerance for cation vacancies without mayor structural reorganisation, as evidenced by X-ray diffraction and solid-state nuclear magnetic resonance spectroscopy. Measurements of the electric properties reveal that Cu$_{3-x}$P is a bad metallic *p*-type conductor. The resistivity is composition-dependent and displays a distinct anomaly from a phase transition, leading to the discovery and structural characterisation of two hitherto unknown low temperature polymorphs. Electrochemical evaluation of copper-deficient Cu$_{3-x}$P as anode material for lithium ion batteries reveals a drastic change in the cycling mechanism leading to an increase of the initial capacities by about 70 %. This work gives a comprehensive insight into the chemical and structural features of copper-deficient Cu$_{3-x}$P and should lead to an improved understanding of its properties, not only for battery applications.

INTRODUCTION

Metal phosphides are well-known for their interesting structural diversity and their large variation of useful physical properties.[1–4] Among this group of phosphides, copper(I) phosphide Cu$_{3-x}$P is one binary representative. Although its crystal structure has been already reported in the 1970s by Olofsson,[5] scientific interest has only emerged at the beginning of the 21st century, and subsequently several applications have been developed. Cu$_{3-x}$P can be used, for example, as an oxygen scavenger during the production of copper and its alloys[6–9], as anode material in lithium ion batteries[10–18], and as catalyst for the splitting of water[19–32]. Especially the latter example has lately attracted a lot of attention.

Despite this emerging interest, full characterisation and understanding of the structural features of this phosphide are yet to be completed. In particular, it is still frequently considered to have the idealized "Cu$_3$P" composition, although Olofsson had postulated partially occupied copper positions in the crystal structure.[5] This evidence was further substantiated experimentally[33] and theoretically[34], and confirmed by us recently.[35] However, the impact of this structural feature is not yet widely considered in many investigations, although there are even a few studies using the copper deficiency for application. It was found, for example, that copper vacancies are responsible for plasmonic absorption features of Cu$_{3-x}$P nanocrystals in the near-infrared, which were used for constructing flexible photodetectors.[34,36,37] The full potential of this material, however, can only be explored if Cu$_{3-x}$P with defined and chosen composition is accessible. Unfortunately, robustly reproducible synthetic protocols have not been reported so far.

Recently, we reported an ionothermal route to synthesize single-phase Cu$_{2.95(4)}$P by direct reaction of copper metal and red phosphorus (P$_{red}$) in ionic liquids (ILs). Although this synthesis is simple and capable of producing large quantities of high-quality copper-rich Cu$_{3-x}$P in a comparatively short time, the drawback of this method is the formation of X-ray amorphous CuP$_2$ as a second phase when Cu$_{3-x}$P with $x \geq 0.1$ is targeted.[35] As evidenced by nuclear magnetic resonance (NMR) spectroscopy, a crucial step during this ionothermal synthesis is the chemical activation of P$_{red}$. In particular, small quantities of P$_4$ molecules are formed when P$_{red}$ is heated in trihexyltetradecylphosphonium chloride ($[P_{66614}]Cl$).[38] This initial finding suggested that white phosphorus (P_{white}) might be an even better phosphorus precursor in the synthesis of $Cu_{3-x}P$, which we subsequently evaluated in this work.

Here we report our results on the syntheses of copper-deficient $Cu_{3-x}P$ ($x > 0.1$) *via* the reaction of copper and P_{white} in different ILs. The use of P_{white} in chloride-containing ILs suppresses the formation of CuP_2 impurities thus making single-phase $Cu_{3-x}P$ ($0.1 < x < 0.7$) accessible. Furthermore, we shed light on the relationship between the crystal structure and a selection of composition-dependent physical properties, hence demonstrating that the control of the $Cu_{3-x}P$ composition is crucial for possible applications to lithium ion batteries.

EXPERIMENTAL SECTION

Starting Materials. All compounds were handled in an argon-filled glovebox (M. Braun; $p(O_2)/p^\circ < 1$ ppm, $p(H_2O)/p^\circ < 1$ ppm). The ILs trihexyltetradecylphosphonium chloride ($[P_{66614}]Cl$, IoLiTec, >95 %), trihexyltetradecylphosphonium bromide ($[P_{66614}]Br$, IoLiTec, >95 %), Trihexyltetradecylphosphonium bis(trifluoromethylsulfonyl)imide ($[P_{66614}][NTf_2]$, IoLiTec, >98 %) and trihexyltetradecylphosphonium acetate ($[P_{66614}][OAc]$, own synthesis) were dried at 110 °C for 12 h under dynamic vacuum. Copper (ABCR, 99.9 % and 99.999 %, spherical, 100 mesh) was treated with H_2 at 400 °C before use. Following a procedure described by Brauer, P_{red} (ABCR, 99.999 %) was washed with sodium hydroxide, rinsed with refluxing water, and finally dried under vacuum.[39] P_{white} was obtained by heating the purified P_{red} in an evacuated silica tube to 450 °C. The opposite side of the ampoule protruded from the tubular furnace to allow condensation of P_{white}. The crude product was collected under argon and sublimed twice in an evacuated silica tube at 100 °C until a transparent waxy solid was obtained. P_{white} is a hazardous form of the element. It is spontaneously combustible upon exposure to air and extremely toxic (estimated human lethal dose: 50-100 mg).

Synthesis of $[P_{66614}][OAc]$. The IL was synthesized *via* anion metathesis. $[P_{66614}]Cl$ (20.8 g, 40 mmol) and K[OAc] (4.9 g, 50 mmol) were dissolved separately in 20 mL and 50 mL ethanol, respectively. Upon mixing of both solutions, potassium chloride precipitated immediately as a fine white solid. The solution was allowed to stir over night before KCl was filtered off leading to a transparent yellow solution. Subsequently, the ethanol was removed with a rotary evaporator. In the course of this procedure, the excess of K[OAc] precipitates forming a cloudy dispersion. Due to the low viscosity the solid can easily be filtered, leading to a transparent light-yellow filtrate. Finally, the product was dried as stated above. It must be noted, however, that this anion metathesis is not expected to yield quantitative chloride-to-acetate exchange.

Synthesis of $Cu_{3-x}P$ ($0.1 < x < 0.7$). In a glovebox, stoichiometric amounts of copper and P_{white} (total mass ≈ 200 mg) were carefully weighed directly into a glass flask containing a magnetic stirring bar. The starting materials were covered with 1300 mg of $[P_{66614}]Cl$ (7.5 mmol) and the flask was subsequently sealed with a glass stopper. The flask was rapidly heated to 200 °C in an oil bath and stirred vigorously for 24 h. After cooling to room temperature, the mixture was dispersed in ethanol using an ultrasonic bath and subsequently centrifuged. The solvent was then decanted and discarded. The washing procedure was repeated three times. The resulting fine greyish powder was dried under ambient conditions. To avoid surface oxidation, the material was alternatively washed in a glovebox with dried dichloromethane, provided by a solvent purification system (M. Braun), and dried under argon atmosphere. $Cu_{3-x}P$ is obtained in yields of 99+ %.

Crystal Growth of $Cu_{3-x}P$. Single-crystals suitable for crystal structure determination were obtained by annealing polycrystalline $Cu_{3-x}P$ at high temperature. A sample of $Cu_{3-x}P$ (≈ 100 mg) with the nominal composition of $Cu_{2.7}P$ was synthesized and dried under argon as described above. In a glovebox, it was transferred into a silica tube, which had previously been dried under dynamic vacuum at 1000 °C for 1 h. After sealing the silica tube under vacuum, the sample was annealed at 900 °C for 2 weeks in a chamber furnace. Adding a small amount of I_2 notably accelerated the recrystallization process. The resulting solid was gently ground to obtain shiny black polyhedra of $Cu_{3-x}P$. Energy dispersive X-ray (EDX) spectroscopy showed no iodine in the $Cu_{3-x}P$ crystals.

Elemental Analysis. The $Cu_{3-x}P$ samples were dissolved in *aqua regia* with the assistance of microwave irradiation and subsequently diluted with water. The determination of the Cu/P ratio was performed with inductively coupled plasma optical emission spectroscopy (ICP-OES) using a 5100 SVDV (Agilent). The measurement of every sample was independently repeated at least three times.

Powder X-ray Diffraction. Powder X-ray diffraction (PXRD) was performed at 296(1) K on an X'Pert Pro MPD diffractometer (PANanalytical) equipped with a curved Ge(111) monochromator using $CuK\alpha_1$ radiation ($\lambda = 154.056$ pm). Le Bail analysis was performed with the software package Jana2006[40,41] using an internal LaB_6 standard (660b, National Institute of Standards and Technology, USA).

Scanning Electron Microscopy. The dried as-prepared samples were dispersed in ethanol, and a few drops were placed on a polished silicon wafer. After evaporation of the ethanol, the wafer was fixed on a sample holder with a graphite pad. Scanning electron microscopy (SEM) was performed by using an SU8020 (Hitachi) instrument with a triple detector system for secondary and low-energy backscattered electrons (U_e = 3 kV).

Energy-Dispersive X-ray Analysis. The compositions of the samples were semi-quantitatively analyzed with EDX spectroscopy (U_e = 20 kV) using an SU8020 (Hitachi) instrument equipped with a Silicon Drift Detector X-Max^N (Oxford Instruments). Samples were embedded into an epoxy polymer (EpoThin^{TM} 2, Buehler) under vacuum. The pellets were then wet-ground with a MetaServ 250 (Buehler, SiC grinding paper) and subsequently polished with a fleece on the same machine using an alumina suspension (MasterPrep^{TM}, Buehler). After coating the polished pellets with carbon, they were fixed on the sample holder with a graphite pad. With respect to the preparation method, the elements C, O and Cl (both of the polymer and the coating) as well as Al (from the polishing suspension) were omitted in EDX quantifications.

Crystal Structure Determination. Suitable single-crystals (shiny black polyhedra) were selected with the help of a light microscope in a glovebox. The crystals were attached to 0.2 mm glass capillaries and sealed in larger ones of 0.5 mm diameter to prevent oxidation during the measurements. Temperature dependent screening measurements and complete data sets were recorded on a SuperNova diffractometer (RigakuOxford Diffraction) using graphite-monochromated MoKα radiation (λ = 71.073 pm) with a microfocus source. Lorentz factor, polarization, and multi-scan absorption corrections were applied. The structure at 300 K ($Cu_{3-x}P$ (*hP*24)) was solved by charge-flipping[42,43]; atomic coordinates of the low-temperature phases at 200 K ($Cu_{3-x}P$ (*hP*96)) and 80 K ($Cu_{3-x}P$ (*tP*288)) were developed by group-subgroup relations, *cf.* discussion. Structure refinements were performed with Jana2006.[40,41] Graphical representations of the structures were drawn with the program Diamond.[44] Crystallographic data of the three polymorphs is summarized in Table S6, the respective atom parameters are stated in Tables S7 – S9. Further details about the crystal structures can be obtained from the Fachinformationszentrum Karlsruhe, 76344 Eggenstein-Leopoldshafen (Germany) on quoting the depository numbers CSD-434583 ($Cu_{3-x}P$ (*hP*24), 400 K), CSD-434584 ($Cu_{3-x}P$ (*hP*24), 300 K), CSD-434585 ($Cu_{3-x}P$ (*hP*96), 200 K) and CSD-434586 ($Cu_{3-x}P$ (*tP*288)), 80 K).

Nuclear Magnetic Resonance Spectroscopy. Liquid samples were transferred into tubes with polytetrafluorethylene valves (Deutero) in a glovebox. The tubes were evacuated and the valves were closed prior to the measurement. To avoid any solvation influences, dimethyl sulfoxide-d$_6$ was provided inside a sealed capillary in the NMR tubes as external lock. The liquid-state NMR experiments were performed using a Bruker AVANCE III HDX, 500 MHz Ascend spectrometer at 333 K. The ^{31}P NMR spectra were recorded at the resonance frequency of 202.45 MHz by using a 5 mm high-resolution CryoProbe Prodigy probe head. Solid-state magic angle spinning (MAS) NMR experiments were performed on a Bruker Ascend 800 MHz spectrometer using a double-resonance 1.3 mm MAS NMR probe operating at the resonance frequency of 323.9 MHz and the MAS frequency of 40 kHz. The chemical shifts were referenced externally to $\delta(H_3PO_4$; 85 %) = 0.00 ppm. For the determination of the chemical shift of signals in the ^{31}P MAS NMR spectra, the centers of gravity of the signals were used

Electron Spin Resonance. For the characterization with electron spin resonance (ESR) spectroscopy, it was required to synthesize $Cu_{3-x}P$ without paramagnetic impurities. The material was therefore prepared with freshly reduced Cu (99.999 %) and the samples were washed and stored in a glovebox. The ESR experiments were carried out with a standard continuous-wave spectrometer at temperatures between 5 K and 300 K. We measured the power (P) absorbed by the sample from a transverse magnetic microwave field at X-band frequency (~9.4 GHz) as a function of an external, quasi-static magnetic field (B). A lock-in technique (modulating the field with 0.5 mT at 100 kHz) was used to improve the signal-to-noise ratio, which yields the derivative of the resonance signal dP/dB.

Electrical Resistivity and Hall Effect Measurements. For the determination of the electronic transport properties, two samples with the compositions $Cu_{2.79(2)}P$ and $Cu_{2.43(5)}P$ were selected. The powders were checked for purity by PXRD and SEM, their compositions were determined by elemental analysis. The fine ground powders were compacted with spark plasma sintering (SPS) using an SPS-515 ET setup (Fuji Electronic Industrial) under a pressure of 100 MPa with the heating rate of 50 K·min^{-1} to the final temperature of 350 °C, which was subsequently held for 10 min until the sample was cooled to RT. PXRD and SEM investigations proved the material to be unchanged after the SPS. Rods of about 8 mm length were cut from the pellets. Thin Pt wires (25 µm) were attached to the samples by spot welding. Resistivity (ρ) was measured in a conventional four-probe arrangement while for the Hall resistivity (ρ_{xy}) a five-wire configuration was used. Measurements were performed using low-frequency alternating current in a measurement system PPMS 9 (Quantum Design, ACT option) with magnetic fields up to B = 9 T and temperatures between 2 K and 300 K. The transverse magnetoresistance $\rho(B)$ and the Hall resistivity ρ_{xy}(B) were measured at fixed temperatures. The $\rho_{xy}(B)$ was found to vary linearly with field up to ± 9 T.

Heat Capacity Measurements. For the heat capacity measurements, the SPS sintered sample with the composition of $Cu_{2.79(2)}P$ was chosen. The sample was crushed and a thin platy piece (1.00 mm x 0.83 mm x 8.24 mm) was selected with the help of a microscope. Heat capacity measurements were conducted on a 9 T CFMS micro-chip calorimeter (Cryogenic Ltd.) using the a. c. method (f = 5 Hz, U = 0.8 V) with Apiezon N grease as thermal contact.

Electrochemical Characterization. To minimize the influence of a possible surface oxidation of $Cu_{3-x}P$, all samples for the electrochemical characterization were washed and handled exclusively under argon atmosphere in a glovebox. For the preparation of the electrodes, 80 wt.% of $Cu_{3-x}P$ and 10 wt.% Super P (Timcal) were mixed in a stainless-steel shaker for 20 min at 25 Hz. The binder solution was prepared by dissolving 10 wt.% PVDF 1013 (Solvay) in N-methylpyrrolidone (NMP). Subsequently, 0.3 ml of the binder solution and 100 mg powder were mixed and sonicated for 30 min. After doctor blading onto a copper foil in a glovebox, the samples were pre-dried overnight at 80 °C. After cutting electrodes of 12 mm in diameter, the electrodes were again dried overnight at 80 °C under vacuum. The Swagelok cells were assembled in an argon-filled glovebox using a two-electrode configuration. Two glass fiber separators (Whatman) and 250 µL electrolyte were placed between a lithium metal disc (Chempur, 250 µm) as counter electrode and the copper phosphide as working electrode. A mixture of 1 M $LiPF_6$ in dimethyl carbonate/ethylene carbonate (1:1 v/v) (Selectilyte LP30, BASF) was employed as electrolyte. Electrochemical tests were conducted at a constant temperature of 25 °C in a climate chamber using a multichannel VMP3 potentiostat (BioLogic). Galvanostatic cycling with potential limitation (GCPL) was performed between 0.7 and 2.0 V vs. Li/Li^+ at a current density of 12 $mA \cdot g^{-1}$ (C/10 for differential capacity plots). The current density and the specific capacity were calculated based on the mass of copper phosphide.

RESULTS AND DISCUSSION

Synthesis and material characterization. The reaction of elemental copper with white phosphorus in $[P_{66614}]Cl$ yielded a greyish powder of single-phase $Cu_{3-x}P$ (0.1 ≤ x ≤ 0.7) according to PXRD (Figure 1) and SEM (Figure S1, Supporting Information). Elemental analysis confirmed that the final composition of the material is in accordance with the targeted nominal composition of the respective synthesis (Table S1, Supporting Information). It was observed that the pristine material is slightly more coarse-grained in comparison to the $Cu_{3-x}P$ obtained from the syntheses with P_{red}[35], but can be easily ground to a fine powder. SEM imaging of the samples reveal agglomerated particles with an average size of approximately 50 µm (Figure 2, left). These particles consist of tiny intergrown platelets (Figure 2, right), which rationalizes the observation that the sample can be crushed easily. It was also found that the tendency of agglomeration increases with the ratio of starting material to IL; hence increasing the total mass of the starting materials whilst keeping the amount of IL constant lead to larger agglomerates (Figure S2, Supporting Information).

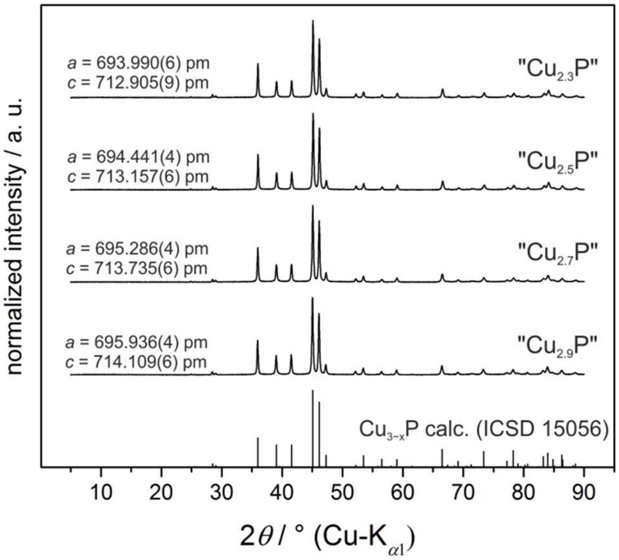

Figure 1. PXRD patterns of $Cu_{3-x}P$ from the reaction of Cu and P_{white} in $[P_{66614}]Cl$ with nominal compositions.

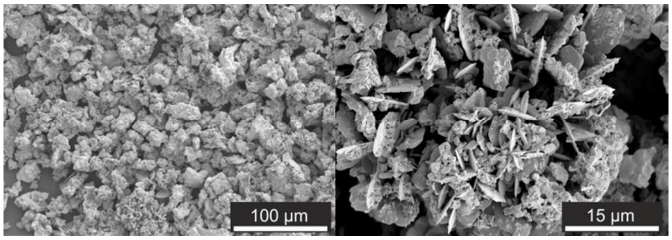

Figure 2. SEM micrographs of $Cu_{3-x}P$ (after washing and drying).

As discussed, the ionothermal synthesis of $Cu_{3-x}P$ (x ≥ 0.1) from P_{red} suffers from the formation of X-ray amorphous CuP_2 as a byproduct.[35] As shown in Figure 3, a sample of the nominal composition $Cu_{2.5}P$ synthesized with P_{red} exhibits a large amount of the amorphous CuP_2 as impurity, which appears dark relative to the $Cu_{3-x}P$ main phase in SEM images captured with a back-scattered electron detector (BSE) and shows a notable difference in composition as evidenced by EDX spectroscopy.[35] In contrast, CuP_2 is not detectable if the synthesis is conducted with P_{white} leaving all other reaction parameters unchanged. This finding is supported by the results of the solid-state ^{31}P NMR experiments and the Le Bail fittings of the X-ray diffraction data. As reported recently, $Cu_{3-x}P$ exhibits a composition dependent Knight shift, which is proportional to the change of the unit cell dimensions. Both can easily be used to track the change of the $Cu_{3-x}P$ composition.[35,45] Comparing $Cu_{3-x}P$ samples from P_{red} and P_{white} precursors with the same nominal composition reveals a significant downfield shift of the solid-state NMR signal and a smaller unit cell volume for all samples synthesized with P_{white} (Figure 4). This indicates that $Cu_{3-x}P$ samples

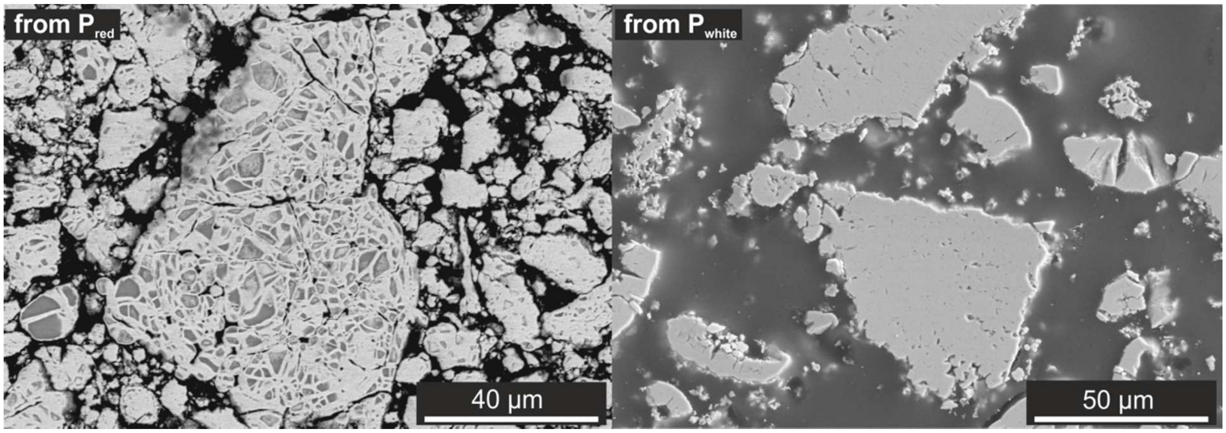

Figure 3. SEM (BSE) micrographs of $Cu_{3-x}P$ synthesized from a molar ratio Cu:P = 2.5:1 with P_{red} (left) and P_{white} (right). *Bright areas*: $Cu_{3-x}P$; *dark areas*: CuP_2; *black areas*: organic polymer.

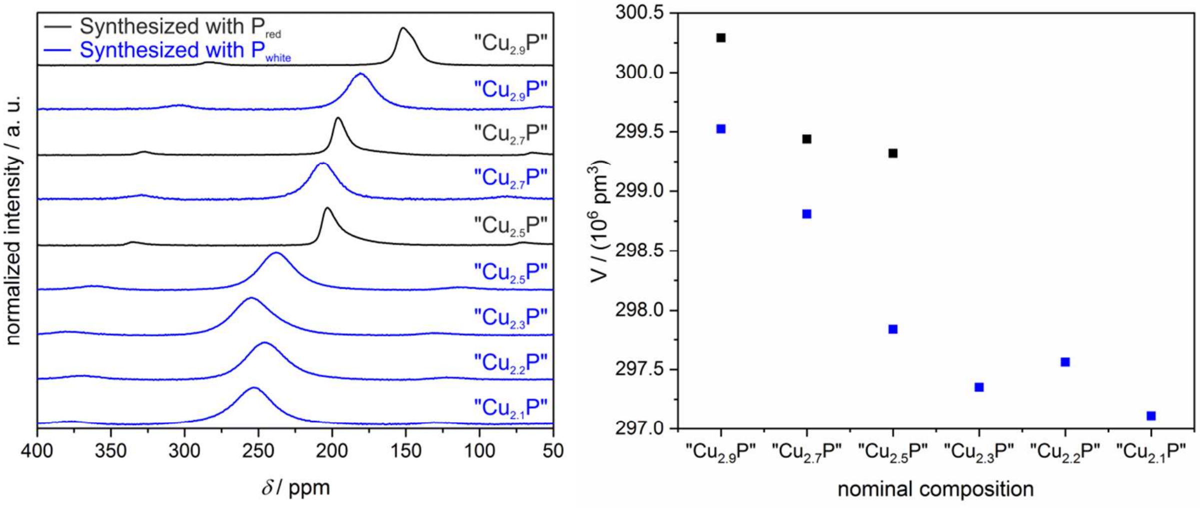

Figure 4. ^{31}P MAS NMR spectra (left) and unit cell volumes fitted from the PXRD data (right) of $Cu_{3-x}P$ with different nominal compositions. *Black symbols*: samples synthesized with P_{red}. *Blue symbols*: samples synthesized with P_{white}. For detailed data see Table S2, Supporting Information.

obtained from reactions with P_{white} exhibit a higher Cu:P ratio than their counterparts synthesized from P_{red}, because no phosphorus is consumed by the formation of the undesired phosphorus-rich CuP_2 impurity. The shapes of the ^{31}P solid-state NMR signals of the $Cu_{3-x}P$ samples differ significantly depending on which allotrope of phosphorus was used as starting material. $Cu_{3-x}P$ synthesized from P_{red} exhibits narrow but asymmetric signals whilst samples obtained from P_{white} show broad isotropic signals. This broadening can most likely be attributed to the presence of $Cu_{3-x}P$ phases with slightly different compositions in one batch, pointing towards a high compositional homogeneity if the synthesis is conducted with P_{red} and rather low homogeneity if P_{white} is used. This is in agreement with the results of the EDX analysis. While the $Cu_{3-x}P$ from P_{red} shows a very homogenous composition across the sample,[35] we found the composition of different $Cu_{3-x}P$ crystallites varying slightly if P_{white} is used as indicated by a higher standard deviation of the average composition (Figure S3 and Table S3, Supporting Information). The copper-poor limit of $Cu_{3-x}P$ seems to be reached at $x = 0.7$ with the synthesis method presented in this work. This is, on the one hand, indicated by the ^{31}P NMR shift, which does not change significantly beyond this composition. Additionally, fluctuations in the NMR shifts and in the lattice constants were found if $Cu_{3-x}P$ ($x > 0.7$) was targeted leading to poorly reproducible results, however, the exact reason for this behavior requires further studies. Attempts to synthesize $Cu_{2.1}P$ using P_{white} lead to the formation of CuP_2 impurities in the product (Figure S4 and Table S4, Supporting Information) as it was previously observed for the synthesis with P_{red}.

The impact of different phosphorus allotropes on the phase formation. Our results demonstrate that the co-formation of CuP_2 inevitably leads to copper-richer (*i.e.* phosphorus-poorer) $Cu_{3-x}P$ phases. Therefore, the key challenge for the synthesis of copper-deficient $Cu_{3-x}P$ is to suppress the CuP_2 formation. This applies not only to IL-

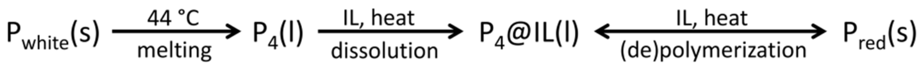

Figure 5. Mobilization of the discussed phosphorus allotropes in $[P_{66614}]Cl$ at elevated temperatures as evidenced by NMR spectroscopy (s = solid; l = liquid).

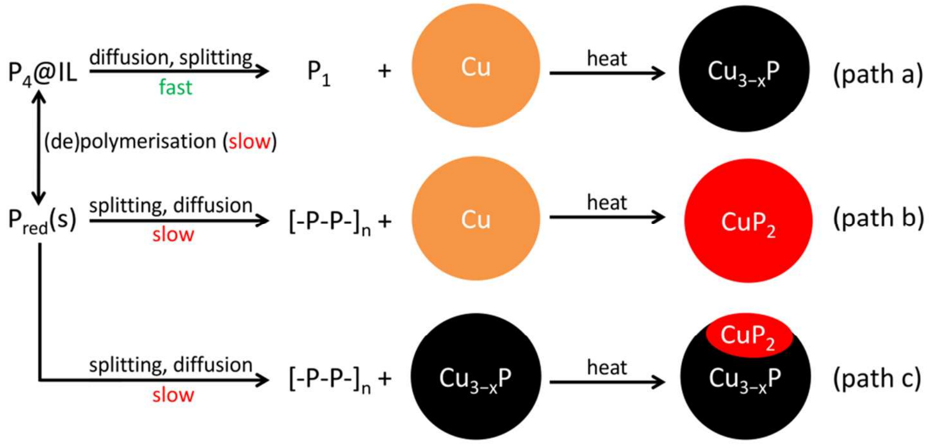

Figure 6. Scheme of the proposed mechanism of the $Cu_{3-x}P$ and CuP_2 formation in $[P_{66614}]Cl$.

based syntheses at low temperatures, as similar phase relations have also been observed in high-temperature solid-state approaches.[5,33,46] Our results suggest that under ionothermal conditions CuP_2 is effectively suppressed if P_{red} is substituted by P_{white}, which should be attributed to their different allotropic structures and, consequently, their chemical properties. White phosphorus, which consists of P_4 molecules, is highly reactive (*e.g.* spontaneous ignition in air) and soluble in many organic solvents.[47–50] White phosphorus, which consists of P_4 molecules, is highly reactive (*e.g.* spontaneous ignition in air) and soluble in many organic solvents.[47–50] In contrast to that, the polymeric structure of P_{red} is far less reactive, stable in air, and almost insoluble in a majority of common solvents.[51] However, it must be considered that our ionothermal reactions are conducted at approximately 200 °C in an ionic liquid medium. It is therefore crucial to discuss the ways in which the phosphorus precursors are mobilized and changed under the impact of temperature and the IL.

At the reaction temperature P_{white} is already molten ($T_m(P_{white})$ = 44.1 °C)[51] and the P_4 molecules are partially dissolved in the IL as evidenced by NMR spectroscopy.[38,52] This means, the P_4 molecules are homogenously distributed within the reaction medium and diffusion is not rate-determining, especially if of the reaction mixture is continuously stirred. Extensive heating of P_4, on the other hand, initiates its polymerization to P_{red} (Figure S5 and Figure S6, Supporting Information), hence decreasing the reactivity of the precursor. *Vice versa*, it was found that P_{red} dissolves slowly as P_4 if heated inside the reaction medium, which consequently increases the reactivity of the precursor (Figure 5).[38,52] It should be noted, that we only have experimental evidence for P_4 molecules as mobile species, but we cannot exclude the presence of larger fragments, *e.g.* phosphorus nanoparticles[54], which are currently not detectable with NMR spectroscopy undergone in this work.

These results demonstrate the impact of the reactivity of the different precursors on the phase formation of $Cu_{3-x}P$, which is mainly attributed to the rate mobile P_4 molecules are provided. Furthermore, we assume that these different reaction behaviors are also related to the crystal structures of $Cu_{3-x}P$ and CuP_2. The crystal structure of $Cu_{3-x}P$ hosts isolated P atoms (or P^{3-} ions if we consider the ionic limit) without P–P bonds,[5] and the formation of the phase requires a consecutive splitting of the phosphorus precursors into "P_1" moieties at the reaction sites. This requires less energy when starting from P_4 molecules than from the polymeric phosphorus network of P_{red}, and we consequently assume that $Cu_{3-x}P$ is preferably formed by P_4 molecules (Figure 6, path a).

On the other hand, the comparatively slow decomposition of P_{red} creates a "bottle neck" effect in the reaction leading to considerable amounts of unreacted P_{red} amongst the emerging $Cu_{3-x}P$ particles. We assume that the presence of unreacted P_{red} is causing the formation of CuP_2, as an extended covalent phosphorus network is found in the crystal structure of this phase,[54,55] and it seems reasonable that CuP_2 is preferably formed if existing P–P bonds are available (Figure 6, path b). Moreover, it is known from the synthesis of polyphosphides that $Cu_{3-x}P$ can be further phosphidized by P_{red},[56] which makes a reaction of $Cu_{3-x}P$ with unreacted P_{red} also probable (Figure 6, path c). The formation of CuP_2 at high P_4 concentrations, on the other hand, is reasonably explained by the aforementioned polymerization of P_4, which leads to the extended formation of P–P bonds. However, the rate of the CuP_2

formation in all these cases is limited due to slower solid-solid diffusions involved in these reactions, which may explain why $Cu_{3-x}P$ nevertheless appears as the main phase.

The impact of the ionic liquid anion on the phase formation and the activation of phosphorus. The question remains what excatly the role of the IL is during $Cu_{3-x}P$ formation and how it affects the proposed mechanism. Our previous results indicated that the cation does not have a notable influence on the phase formation. In contrast to that, the anions appear to have considerable impact.[35] This can be clearly demonstrated if the $Cu_{3-x}P$ synthesis is attempted in $[P_{66614}][NTf_2]$ (Figure 7). The reaction of copper and P_{red} in this IL is almost completely inhibited, evidenced by the detection of only elemental copper in the PXRD of the solid reaction product. Only the sample surface turns slightly dark during the reaction, most likely due to the formation of an X-ray amorphous phosphide coating. The reaction of copper with P_{white} under the same conditions, on the other hand, leads to the formation of $Cu_{3-x}P$, although elemental copper is still present in the product.

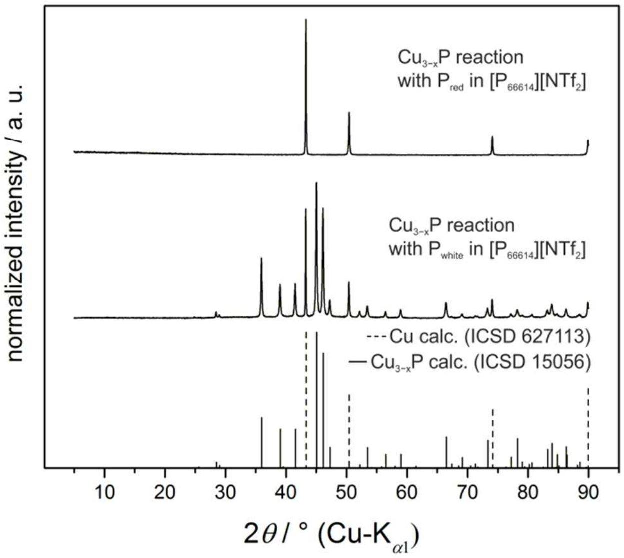

Figure 7. PXRD patterns of the products of reacting Cu and P_{red} (top, molar ratio Cu:P = 2.95:1) as well as Cu and P_{white} (bottom, molar ratio Cu:P = 2.7:1) in $[P_{66614}][NTf_2]$.

To further evaluate the differences of these two anions, a series of $Cu_{3-x}P$ model reactions with P_{white} were conducted in $[P_{66614}]Cl/[P_{66614}][NTf2]$ mixtures (Figure 8, left). The results of the PXRD measurements prove that already 5 mol% of chloride in the reaction mixture lead to a drastic improvement of the phase formation, in particular, no elemental copper can be detected in the products anymore. Remarkably, SEM investigations of the reaction products (Figure 8, right) reveal the formation of X-ray amorphous CuP2, indicated by dark spots in the back-scattered electron images, which only vanish if 60 mol% or more chloride-anion IL is used in the reaction.

Evidently, chloride ions facilitate the reaction and act as a mineralizer in the same way as has been reported for halide ions in the solid-state synthesis of the aforementioned polyphosphides.[56] Apparently, this mineralizer concept can be transferred to the ionothermal syntheses as well. Similar findings have been already reported by the group of Dehnen, who demonstrated the positive impact of chloride on the crystallization of chalcogenidometalate superspheres.[57]

Besides this mineralizing effect, high concentrations of chloride ions seem to prevent the formation of P–P bonds and, thus, inhibit the formation of the CuP_2 impurities. The latter effect is closely related to what we have discussed in the previous section. The phosphorus precursor has to be split at the reaction site, which obviously requires a certain amount of chloride as catalyst. If the P–P bonds are not sufficiently activated, the reaction follows the pathways for polyphosphides, ultimately leading to the formation of CuP_2.

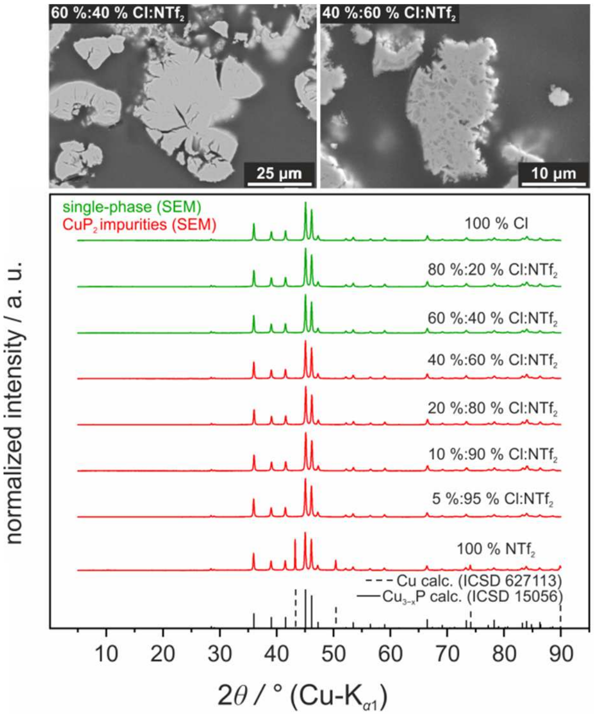

Figure 8. PXRD patterns (left) and SEM-BSE micrographs (right) of the products of reacting Cu and P_{white} (molar ratio Cu:P = 2.7:1) in different $[P_{66614}]Cl/[P_{66614}][NTf_2]$ mixtures. The molar ratios of the anions in these mixtures are given in the figure.

Conducting the same model reaction in $[P_{66614}]Br/[P_{66614}][NTf_2]$ mixtures reveals the mineralizing effect also for bromide anions, although CuP_2 was found in the product already after reducing the bromide content in the reaction mixture to 80 mol% (Figure S7, Supporting Information). Hence, bromide seems less effective in activating P–P bonds.

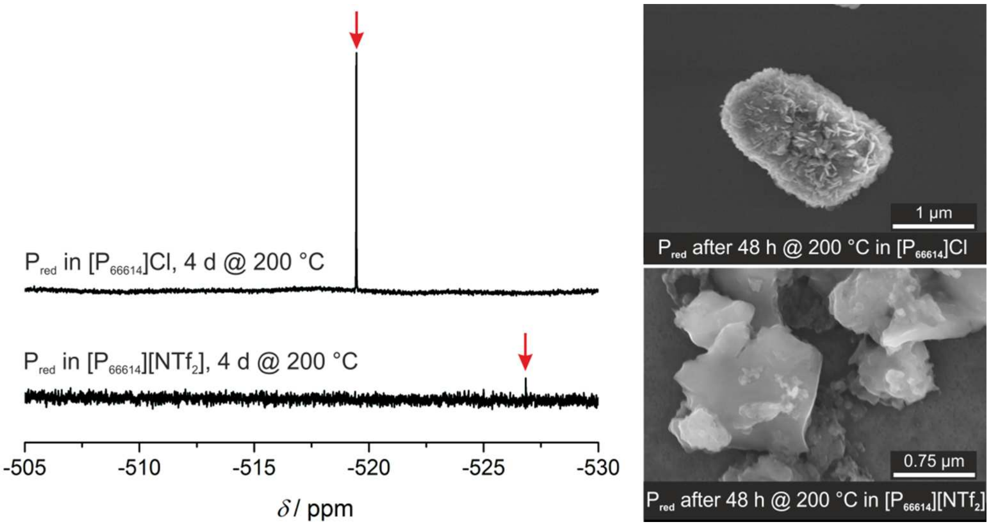

Figure 9. Sections of the ^{31}P NMR spectra of different ILs after heating with P_{red} (left) and SEM micrographs of Pred particles after heat treatment in different ILs (right). The red arrow marks the NMR resonance of P4 in both ILs. For full spectra, see Figure S8 and S9, Supporting Information.

The different reactivities of chloride, bromide and $[NTf_2]^-$ may be explained by their different nucleophilicity or Lewis basicity. P_4, which is known for its electrophilic character, can readily be attacked by nucleophiles.[49] This reactivity is, however, not limited to P_4 but is also found for P_{red}, where nucleophilic attacks on the phosphorus network lead to a cascade of disproportionation reactions and rearrangements. For example, P_{red} is degraded by K[OEt] and the polyphosphide anions $P_{21}{}^{3-}$, $P_{16}{}^{2-}$, and $P_5{}^-$ are obtained.[58] The nucleophilicity of dissolved anions, on the other hand, depends on the nature of the solvent. In protic solvents, the nucleophilicity of halide anions decreases in the series $I^- > Br^- > Cl^- > F^-$ due to the strong solvation of the smaller halide ions. In aprotic solvents, however, this trend is inverted and fluoride becomes the strongest nucleophile.[59] This trend for aprotic solvents is in general also found for ILs, as demonstrated mainly for alkyl-substituted imidazolium compounds[60–62] The $[P_{66614}]^+$ cation was found to interact even less with anions than any imidazolium cation, owing to its increased steric hindrance and decreased potential to form hydrogen bonds.[61] Regarding the different natures of the anions, chloride can be considered to be one of the strongest and $[NTf_2]^-$ one of the weakest nucleophiles within the commercially available ILs.[61,62]

The influence of different anions on the decomposition of red phosphorus has been tested, as the aforementioned decomposition yields P_4 which can qualitatively be followed by NMR spectroscopy.[38] Indeed, we found that the degradation of P_{red} upon heating in the IL under vacuum for several days is far less pronounced in $[P_{66614}][NTf_2]$ compared to $[P_{66614}]Cl$, evidenced by a smaller P_4 signal in the ^{31}P NMR spectrum (Figure 9, left). Moreover, SEM micrographs reveal the surface of P_{red} to be strongly etched in $[P_{66614}]Cl$, as indicated by the rough surface of the red phosphorus particles (Figure 9, right). In contrast, the surface of P_{red} remains unaffected after being heated in $[P_{66614}][NTf_2]$, explaining the distinctively hindered $Cu_{3-x}P$ formation in this IL. Notably, no differences were observed with NMR spectroscopy when P_{red} was heated in $[P_{66614}]Br$ or $[P_{66614}]Cl$. However, the formation of CuP_2 in the product after reducing the amount of $[P_{66614}]Br$ in the reaction mixture demonstrates the lower nucleophilicity of bromide compared to chloride.

These results suggest that the reactivity might be influenced or even tuned by other anions as well. However, the application of stronger nucleophiles in ILs is limited by the stability of the organic cation, especially at higher temperature.[63] Nevertheless, we found that P_{red} can be degenerated by $[P_{66614}][OAc]$ yielding a dark red-colored solution, which is caused by traces of the $[P_{16}]^{2-}$ polyanions as evidenced by NMR spectroscopy (Figure S10, Supporting Information).

Electrical transport properties. $Cu_{3-x}P$ with small x was found to be a metallic conductor at room temperature already several decades ago.[9,64] We recently confirmed the metallic nature of this compound down to 4 K.[35] However, due to a lack of high-quality data, we decided to reinvestigate the electronic transport properties and to extend our characterization to $Cu_{3-x}P$ with lower copper content. The temperature and magnetic field dependence of the electrical resistivity $\rho(B,T)$ and of the Hall resistivity $\rho_{xy}(B,T)$ were determined for compacted polycrystalline samples of $Cu_{2.79(2)}P$ and $Cu_{2.43(5)}P$.

Both samples were found to exhibit metallic *p*-type conductivity with electrical resistivity values at room temperature of 100 and 140 μΩ·cm, respectively. Upon cooling (Figure 10), an anomalous decrease of the resistivity is observed to below 190 K ($Cu_{2.79(2)}P$) or 180 K ($Cu_{2.43(5)}P$) indicating a phase transition. The electric resistivity is lower below the phase transition (more pronounced for the copper-richer phase), suggesting a decrease of the scattering of the charge carriers. Upon heating, the anomalies in both samples are observed at slightly higher temperatures (Figure 10, inset left), hinting at a first order structural phase transition. The transition is accompanied by an anomaly of the heat capacity $C_p(T)$ at this temperature (for $Cu_{2.79(2)}P$, see Figure S13, Supporting Information).

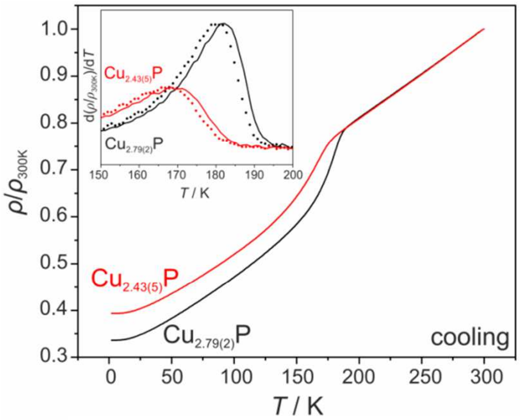

Figure 10. Normalized electrical resistivity of two different $Cu_{3-x}P$ samples. The inset shows the derivative of the resistivity for both samples while cooling (symbols) and heating (lines). For more detailed resistivity curves, see Figure S11 and S12, Supporting Information.

The magnetoresistance is positive and small and increases with decreasing temperature. At $T = 2$ K it attains +5.8 % in a field of 9 T. The Hall coefficient $R_H(T)$ (Figure S14, Supporting Information) as derived from the slopes of $\rho_{xy}(B,T)$ is very similar for both compositions and varies weakly with temperature between $1{\cdot}10^{-9}$ $m^3{\cdot}C^{-1}$ and $2{\cdot}10^{-9}$ $m^3{\cdot}C^{-1}$. Within a one-band model this indicates hole concentrations between $6{\cdot}10^{21}$ cm^{-3} at $T = 2$ K and $3{\cdot}10^{21}$ cm^{-3} at $T = 300$ K, respectively. An impact of the structural phase transition on the carrier concentration is not visible in the Hall coefficient data, which is, however, also due to the small number of data points.

$Cu_{3-x}P$ samples with different compositions were probed by ESR spectroscopy to check if an increasing amount of copper vacancies is mirrored in a partial oxidation of some Cu^+ ions to Cu^{2+}. In accordance with the metallic conductivity we found no evidence for Cu^{2+} in the X-band ESR spectra in the range of 300 K to 5 K (Figure S15, Supporting Information). Thus $Cu_{3-x}P$ probably adopts the variable composition by creating itinerant charge carriers. In this context we must admit, though, that Cu^{2+} cannot always be detected at the X-band frequencies due to spin-phonon interactions.[65]

Temperature-dependent structure investigations. Structural phase transitions of $Cu_{3-x}P$ below ambient temperature, as indicated by the resistivity and Hall measurements, have not yet been reported in literature. Thus, single crystals were grown to investigate the low temperature polymorphs.

Temperature-dependent diffraction data indicated the presence of two low-temperature phases (Figure S16, Supporting Information). For that, diffraction images were taken in steps of 10 K and complete data sets were recorded at 400, 300, 200, 100, and 80 K. The reinvestigation of the crystal structure at 400 K and 300 K confirms the reported Na_3As-type structure in the hexagonal space group $P6_3cm$ (no. 185) with lattice parameters a = 693.5(1) pm and c = 713.0(1) pm (at 295 K) and six formula unit per unit cell.[5] According to its Pearson symbol we call this polymorph $Cu_{3-x}P$ (*hP*24) in the following.

$Cu_{3-x}P$ forms a three-dimensional network structure with Cu–P distances between 232 pm and 249 pm and relatively short Cu–Cu distances of 255 pm to 273 pm. Both, Cu–Cu distances and Cu coordination numbers (Table S5, Supporting Information) bear a resemblance to typical intermetallic phases, like $AuCu_3$[66]. The phosphorus atom exhibits an unusual high coordination number of 11.

For simplicity, the structure can formally be divided in two different layers that alternate along the [001] direction. Slightly puckered honeycomb nets are formed by Cu1, Cu2 (Wyckoff site 2*a* and 4*b*, respectively) and phosphorus atoms. The Cu3 and Cu4 atoms (Wyckoff sites 6*c*) form a strongly corrugated honeycomb net, topologically resembling the structure of grey arsenic (Figure 11). In agreement with de Trizio *et al.*[34], only the latter Cu positions were found to be partially occupied (Table S7, Supporting Information).

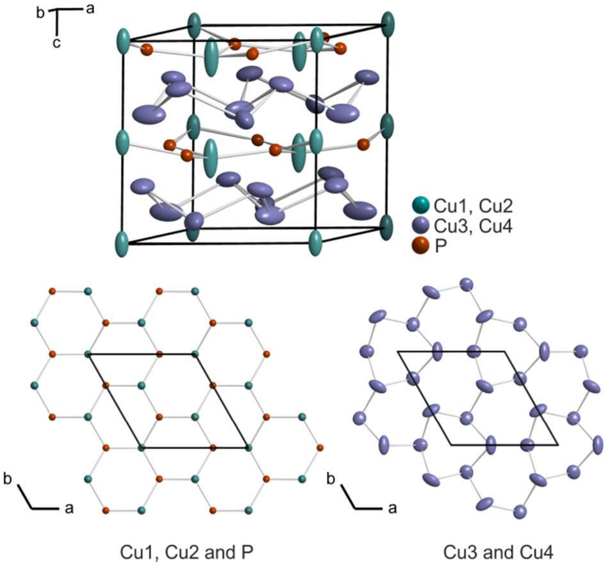

Figure 11. The $Cu_{3-x}P$ (*hP*24) crystal structure (300 K data). The ellipsoids represent 90 % probability.

As visible from Figure 11, Cu3 and Cu4 atoms have large displacement parameters in the hexagonal *ab*-plane whereas the displacements of Cu1 and Cu2 atoms are conspicuous along [001]. The conventional refinement with anisotropic displacement parameters taking the statistical copper vacancies on the Cu3 and Cu4 positions into account resulted in reasonable *R*-values but exhibited large atomic displacement values for all Cu atoms and two pronounced peaks in the difference Fourier maps close to the Cu1 and Cu2 positions. The displacement parameters of all Cu atoms are elongated, those of Cu1 and Cu2 along [001], Cu3 and Cu4 in the *ab*-plane (Figure 11). The extrapolation of the principal mean square displacement parameters to $T = 0$ K indicates mainly dynamic contributions so that an anharmonic refinement with up to 4th rank tensors were considered. To minimize correlations, tensor components were set to zero if the refined parameters were within a standard uncertainty of 3σ. As a results, the *R*-values dropped considerably and the difference *Fourier* map became featureless (Table S6, ESI†). The displacement and occupational parameters of P are unsuspicious. The occupations of the Cu3 and Cu4 positions refined to 88(1) % and 90(1) %, respectively, leading to a composition $Cu_{2.79(1)}P$ in good agreement to the initial composition of the $Cu_{3-x}P$ powder used for growing the single crystals. It should also be noted, that (twin) refinements in subgroups of $P6_3cm$ without *c*-glide planes ($P6_3$, $P3m1$, etc.) do not lead to smooth *Fourier* maps and inconspicuous displacement parameters.

Upon cooling below 260 K additional reflections indicated a doubling of the hexagonal *a* and *b* lattice parameters (Figure S16, center, Supporting Information). As the symmetry of the diffraction image and the reflection conditions remain unchanged, the cell enlargement can be described by an isomorphic symmetry reduction of index 4 and a starting model for the this superstructure was established using the group-subgroup formalism starting from the $Cu_{3-x}P$ (*hP*24) structure model (Figure S17, Supporting Information)[67–69]. The resulting low-temperature structure is called $Cu_{3-x}P$ (*hP*96) in the following.

Noticeably, the Wyckoff positions of Cu1 and Cu2 of the $Cu_{3-x}P$ (*hP*24) structure split into two non-equivalent sites in the low-temperature $Cu_{3-x}P$ (*hP*96) structure and the P, Cu3, and Cu4 positions split into three sites each.

The $Cu_{3-x}P$ (*hP*96) structure model displays similar large and elongated displacement parameters for the Cu atoms so that an anharmonic refinement was performed again. The main difference between $Cu_{3-x}P$ (*hP*24) and $Cu_{3-x}P$ (*hP*96) structures is, however, that the Cu deficit accumulates on one copper site in the low-temperature polymorph $Cu_{3-x}P$ (*hP*96): the refined occupancy for this position, Cu3*a*, is only 25(1) % whereas all other Cu position are fully occupied within a 3σ uncertainty. In other words, a rearrangement of vacancies in the Cu substructure occurs upon cooling (Figure 12).

The composition was computed to $Cu_{2.81(1)}P$ for the $Cu_{3-x}P$ (*hP*96) structure. The coordination polyhedra and interatomic distances of Cu3*a* (occupancy 25%) and Cu3*b* (fully occupied), both derived from Cu3 in the $Cu_{3-x}P$ (*hP*24) structure and adopting the same site symmetry ..*m* (Wyckoff site 6*c*), are hardly distinguishable. As main difference, Cu3*a* exhibits four short Cu-Cu distances of less than 250 pm, whereas for Cu3*b*, all Cu-Cu distances are larger than 260 pm (Figure S19, Supporting Information).

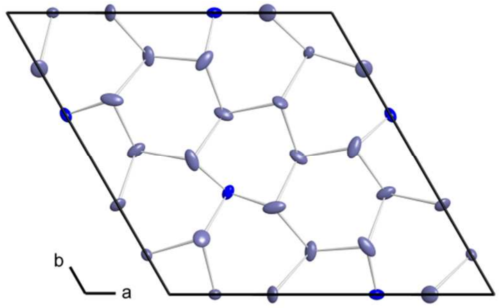

Figure 12. The As-like Cu substructure in $Cu_{3-x}P$ (*hP*96), 200 K data. The Cu atoms marked in dark blue exhibit an occupation of 25(1) %; the others are fully occupied. The ellipsoids represent 90 % probability. For an image of the unit cell content, see Figure S18, Supporting Information.

Upon further cooling below 190 K a second structural reorganization takes place as evidenced by additional satellite reflections at slightly incommensurate positions along *c** (Figure S16, right, Supporting Information). To establish a first structure model of this second low-temperature polymorph, the satellites were indexed using a modulation wave vector $q = (0, 0, 0.31(1))$. Additional diffuse streaks running between the reflections along the *l*-direction were ignored. A starting model was created in the superspace group $P6_3cm(00\gamma)000$ (no. 185.1.24.1)[70] by taking the atomic positions of the $Cu_{3-x}P$ (*hP*96) structure model as average structure. The final refinements were performed using the commensurate option with a threefold *c*-axis resulting in the 3D space group symmetry *P*31*m*. The resulting structure is thus called $Cu_{3-x}P$ (*tP*288) in the following. One harmonic positional modulation wave for all atom positions and for the displacement parameters were refined together with one harmonic wave for the occupation parameters of Cu3*a*. The electron density distribution around the atomic domain of Cu3*a* is clearly disrupted along the modulation direction, mirroring the occupational modulation (Figure 13).

As a consequence, the resulting puckered grey As-like Cu exhibit vacancies in some heights, whereas others are not affected by the positional modulation (Figure 14). In layers with vacancies, the response of the surrounding atoms in terms of positional modulations is much stronger than in fully occupied layers.

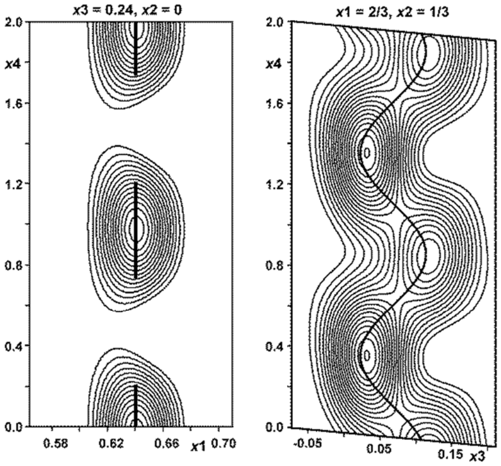

Figure 13. Fourier maps (*F*o) around Cu3*a* of the $Cu_{3-x}P$ (*tP*288) structure indicating the occupational modulation (left) and Cu2*a* with a strong displacement (right); contour lines in steps of 10 e·Å^{-3}, thick black lines represent the calculated atomic positions.

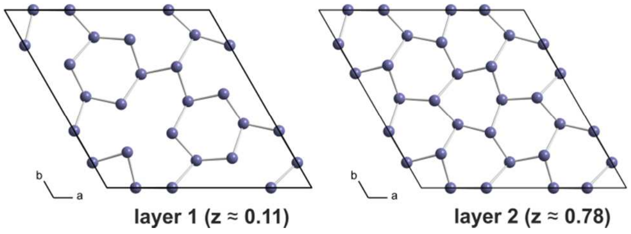

Figure 14. Impact of the Cu modulation on the As-like Cu substructure of $Cu_{3-x}P$ (*tP*288).

Additionally, Cu2*a* exhibits a strong positional modulation along the *c* direction, which may also be interpreted as two Cu positions with alternating occupational modulations. Cu2*a* is generated from Cu2 of the $Cu_{3-x}P$ (*hP*24) structure in the course of the symmetry reductions, which was the atom with the largest displacement parameters along [001] in the $Cu_{3-x}P$ (*hP*24) phase. This is probably due to a certain amount of static disorder underlying the dynamic effects, i.e. local situations where Cu2 is located at slightly different *z*-positions with respect to the plane of the phosphorus atoms.

Considering the omitted diffuse intensities, the refinements converged to acceptable *R*-values for the main reflections and a featureless difference Fourier map. The refined composition of $Cu_{2.85(1)}P$ is in reasonably good agreement with the results of the $Cu_{3-x}P$ (*hP*96) and $Cu_{3-x}P$ (*hP*24) refinements.

The phase transitions are fully reversible. Heating the crystal reveals the same diffraction images and structure models as observed before and during the cooling procedure.

To conclude the crystal structure results, we were able to confirm the proposed copper depleted sites in the $Cu_{3-x}P$ (*hP*24) structure experimentally. Atomic displacement parameters of the Cu atoms indicate a considerable thermal motion. Upon cooling, two polymorphs were discovered that show substantial redistribution of the copper vacancies coupled to a subtle reorganization of the copper partial structure.

Electrochemical characterization. $Cu_{3-x}P$ has been intensively studied as anode material for lithium ion batteries since the beginning of the 21th century, primarily because its volumetric capacity exceeds graphite by a factor of three.[11–14] This advantage initiated a series of detailed mechanistic studies of the $Cu_{3-x}P$ reaction with lithium.[14,15,40,71–73] The following discussion is based on the most recent study of the mechanism with *in situ* ^{31}P and ^{7}Li NMR spectroscopy by Poli *et al.*,[15] which also nicely links in the results of the previous PXRD studies.[46,71]

Based on this recent investigation, copper-rich $Cu_{3-x}P$ reacts with lithium to form three different products, depending on the applied electrochemical potential: (a) $Li_{0.2}Cu_{2.8}P$ (crystal structure unknown); (b) Li_2CuP[33,74] and (c) Li_3P[75,76]. The chemistry behind this substitution can be understood by comparing the known crystal structures in this system (Figure 15). Formally, Li_2CuP is obtained if the Cu^+ ions on the Cu3 and Cu4 positions (Wyckoff site 6*c*) of $Cu_{3-x}P$ are substituted by Li^+. These Cu positions, which are located between layers of buckled $[CuP]^{2-}$ hexagonal nets (including Cu1 and Cu2 positions), were also identified by our crystal structure investigations to host the Cu vacancies of $Cu_{3-x}P$. Following this argument, the structurally unknown $Li_{0.2}Cu_{2.8}P$ should consist of an intermediate structure, where the Cu atoms between the nets are only partially exchanged by Li^+. Upon further lithiation of Li_2CuP, the Cu atoms of the hexagonal nets are fully substituted, leading to the formation of Li_3P.

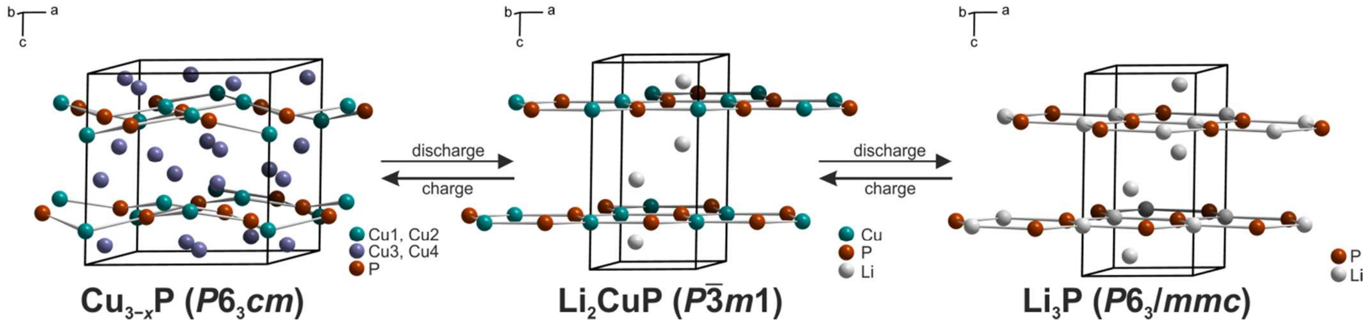

Figure 15. The crystal structures of $Cu_{3-x}P$ and its relation to lithiated phases found within the lithium ion batteries. The chemical bonds outside the hexagonal nets are omitted for clarity. For consistency with literature, the discharging refers to the lithiation and the charging to the delithiation process.

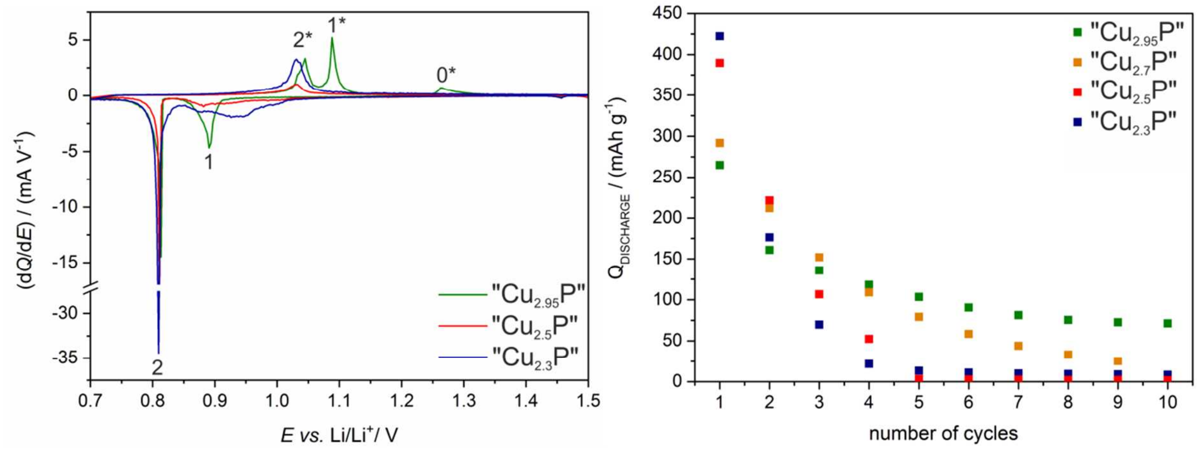

Figure 16. Differential capacity plot of the first cycle (left) and specific capacity plot (right) of different $Cu_{3-x}P$ electrodes. All compositions given are nominal compositions. The processes marked in the differential capacity plot correspond to the reaction equations given in the discussion. For the corresponding voltages profile see Figure S20, Supporting Information.

Lithiation of Li_2CuP, however, requires a more complex reorganization of the crystal structure, which was also found to be disadvantageous in regards to cycling stability.[14] Subsequently, the cut-off potential in our experiments was set to 0.7 V, to prevent the formation of Li_3P and to enable a reversible cycling between $Cu_{3-x}P$ and Li_2CuP. Thus, the following processes should take place:

$Cu_{3-x}P + 0.2\ Li \longrightarrow Li_{0.2}Cu_{2.8}P + 0.2\ Cu$ (process 1)

$Li_{0.2}Cu_{2.8}P + 1.8\ L \longrightarrow Li_2CuP + 1.8\ Cu$ (process 2)

$Li_2CuP + x\ Cu \longrightarrow Li_{2-x}Cu_{1+x}P - Cu^0 + x\ Li$ (process 2*)

$Li_{2-x}Cu_{1+x}P - Cu^0 + x\ Cu \longrightarrow Cu_{3-x}P + x\ Li$ (process 1* + 0*)

We found that electrodes produced from $Cu_{3-x}P$ with various compositions differ significantly (Figure 16). The reaction steps proposed in the mechanism stated above can be accurately assigned to material of a $Cu_{2.95}P$ composition. The differential capacity plots (Figure 16, left) obtained for this material matches those reported in literature.[10,11,14,46] This supports the assumption, that the stoichiometric Cu:P = 3:1 starting ratio in the syntheses ofthese material resulted in the formation of copper-rich $Cu_{3-x}P$. In contrast to that, some features of the lithiation reactions are found less pronounced or missing for $Cu_{3-x}P$ with lower copper content.

Process 1, assigned to the formation of $Li_{0.2}Cu_{2.8}P$, corresponds to the signal found at 0.89 V for $Cu_{2.95}P$. Following the proposed mechanism, this phase should not be formed with $Cu_{2.5}P$ and $Cu_{2.3}P$, as the copper content of these compounds is below that of the targeted phase. This is indeed proven by the absence of the corresponding signal at 0.89 V. Instead, a broad signal is observed for the copper-deficient compounds, which might be caused by small amounts of copper-rich phases present in the investigated samples. Upon further lithiation, the Li_2CuP formation (process 2) is observed for all materials at 0.81 V.

The delithiation of Li_2CuP (process 2*) is found at 1.05 V for all materials, as expected from the results of the first discharge. In the following reaction, further delithiation (process 1* and 0*) is only observed for $Cu_{2.95}P$ at 1.09 V and 1.26 V, respectively. Apparently, there is not enough copper available to form copper-rich phases, which agrees well with the absence of process 1 during the first discharge.

Our results clearly indicate that copper-rich and copper-deficient $Cu_{3-x}P$ reacts differently with lithium. These differences lead to very interesting results in terms of the specific capacity and the cycle stability. The initial capacity of $Cu_{2.3}P$ during the first discharge is about 70 % higher than the capacity of $Cu_{2.95}P$, vice versa the cycling stability of $Cu_{2.95}P$ is much better (Figure 16, right). The performance of our cells can, however, not compete with the excellent results reported by Stan *et al.*[14] This behavior is most likely caused by the coarse-grained material used in our work which could probably be optimized,[10] but was not in the scope of this work. As the higher capacity of the copper-deficient material is counterintuitive to the mechanism discussed in literature,[15] a different lithiation pathway of the copper-deficient material needs to be considered, which should be investigated by more elaborated experiments in the future. Our results, however, suggest that the optimal composition of $Cu_{3-x}P$ for battery applications should not be too close to the stoichiometric Cu_3P composition to enable a high specific capacity and reversible cycling.

CONCLUSION

In summary, we have developed a convenient approach to precisely synthesize different $Cu_{3-x}P$ ($0.1 < x < 0.7$) phases in high yields with excellent reproducibility. Our mechanistic investigations reveal the different mineralizing and activating properties of halide anions in ionic liquids. This is in particular interesting for the development of ionothermal approaches for other inorganic materials, as rules for choosing appropriate ionic liquids are only rarely found in literature. The physical characterization of the $Cu_{3-x}P$ shows a composition-dependent change in the electric conductivity, which is accompanied by a change of the Hall coefficient. The low-temperature phase transition indicated by the non-linear behavior of the electric properties was followed by single-crystal X-ray diffraction elucidating two hitherto unknown $Cu_{3-x}P$ polymorphs. Our analysis of the structural relations of these polymorphs confirms the Cu vacancy accumulation between the Cu/P-layers as suggested in literature.[34] The application of different $Cu_{3-x}P$ phases as anode material in lithium ion batteries evidences a composition-dependent change in the lithiation pathway, which might be used to further optimize these devices.

SUPPORTING INFORMATION

SEM images of $Cu_{3-x}P$, EDX data of $Cu_{3-x}P$, data of elemental analysis of $Cu_{3-x}P$, results of lattice parameter fitting, solid-state NMR data of $Cu_{3-x}P$, photography and solid-state NMR spectra of polymerized P_{white}, PXRD data of $Cu_{3-x}P$, liquid-state NMR spectra of P/IL mixtures, resistivity and Hall data of $Cu_{2.79(2)}P$ and $Cu_{2.43(5)}P$, heat capacity data of $Cu_{2.79(2)}P$, ESR spectra of $Cu_{3-x}P$, crystallographic data, voltage profiles of $Cu_{3-x}P$. This material is available free of charge via the Internet at http://pubs.acs.org.

AUTHOR INFORMATION

Corresponding Author

*E-mail: michael.ruck@tu-dresden.de

Author Contributions

All authors have given approval to the final version of the manuscript.

Funding Sources

This work was supported by the Deutsche Forschungsgemeinschaft (DFG) within the Priority Program SPP 1708. J.J.W. thanks the DFG for funding a Rigaku Oxford Diffraction SuperNova system with a dual source (INST 269/618-1).

Notes

The authors declare no competing financial interest.

ACKNOWLEDGMENT

We would like to thank Dr. F. Haarmann for helpful discussions of the solid-state NMR results. We gratefully acknowledge Dr. G. Auffermann (MPI CPfS, Dresden) for elemental analysis, Dr. I. Veremchuk (MPI CPfS, Dresden) for SPS and V. Charbonneau (IFW, Dresden) for experimental assistance.

ABBREVIATIONS

IL, ionic liquid; P_{red}, red phosphorus; P_{white}, white phosphorus; $[P_{66614}]$, trihexyltetradecylphosphonium; $[NTf_2]$, bis(trifluoromethylsulfonyl)imide; EDX, energy dispersive X-ray; PXRD; powder X-ray diffraction; SEM, scanning electron microscopy; BSE, back-scattered electron; ICP, inductively coupled plasma; OES, optical emission spectrometry; MAS, magic-angle-spinning; ESR, electron spin resonance; SPS, spark plasma sintering; NMP, N-methylpyrrolidone.

REFERENCES

(1) von Schnering, H.-G.; Hönle, W. Bridging Chasm with Polyphosphides. *Chem. Rev.* **1988**, *88*, 243–273.

(2) Pöttgen, R.; Hönle, W.; von Schnering, H.-G. Phosphides: Solid-State Chemistry. In *Encyclopedia of Inorganic Chemistry*, 2nd ed.; King, R. B., Ed.; John Wiley & Sons, Ltd.: Chichester, U.K., 2005; Vol. 8, pp 4255–4308.

(3) Bawohl, M.; Nilges, T. Phosphorus Rich d^{10} Ion Polyphosphides and Selected Materials. *Z. Anorg. Allg. Chem.* **2015**, *641*, 304–310.

(4) Chen, J.-H.; Whitmire, K. H. A structural survey of binary transition metal phosphides and arsenides of the d-block elements. *Coord. Chem. Rev.* **2018**, *355*, 271–327.

(5) Olofsson, O. The Crystal Structure of Cu_3P. *Acta Chem. Scand.* **1972**, *26*, 2777–2787.

(6) Solovyov, S. E. Oxygen Scavengers. In *Kirk-Othmer Encyclopedia of Chemical Technology*; Seidel, A., Bickford, M., Eds.; John Wiley and Sons, Inc.: Hoboken, NJ, 2014; pp 1–31.

(7) Kato, T.; Adachi, S.; Aoyagi, T.; Naito, T.; Yamamoto, H.; Nojiri, T.; Yoshida, M. A Crystalline Metallic Copper Network Application Film Produced by High Temperature Atmospheric Sintering. *IEEE J. Photovoltaics* **2012**, *2*, 499–505.

(8) Adachi, S.; Yoshida, Y.; Nojiri, T.; Kato, T.; Watanabe, S.; Yoshida, M. A reaction mechanism of atmospheric sintering for

copper–phosphorus alloy electrode. *J. Alloys Compd.* **2017**, *695*, 3353–3359.

(9) Robertson, D. S.; Snowball, G.; Webber, H. The Preparation and Properties of Single Crystal Copper Phosphide. *J. Mater. Sci.* **1979**, *15*, 256–258.

(10) Bichat, M.-P.; Politova, T.; Pfeiffer, H.; Tancret, F.; Monconduit, L.; Pascal, J.-L.; Brousse, T.; Favier, F. Cu$_3$P as Anode Material for Lithium Ion Battery : Powder Morphology and Electrochemical Performances. *J. Power Sources* **2004**, *136*, 80–87.

(11) Pfeiffer, H.; Tancret, F.; Bichat, M.-P.; Monconduit, L.; Favier, F.; Brousse, T. Air stable copper phosphide (Cu3P): a possible negative electrode material for lithium batteries. *Electrochem. Commun.* **2004**, *6*, 263–267.

(12) Pfeiffer, H.; Tancret, F.; Brousse, T. Synthesis, Characterization and Electrochemical Properties of Copper Phosphide (Cu$_3$P) Thick Films Prepared by Solid-State Reaction at Low Temperature: A Probable Anode for Lithium Ion Batteries. *Electrochim. Acta* **2005**, 50, 4763–4770.

(13) Chandrasekar, M. S.; Mitra, S. Thin Copper Phosphide Films as Conversion Anode for Lithium-Ion Battery Applications. *Electrochim. Acta* **2013**, *92*, 47–54.

(14) Stan, M. C.; Klöpsch, R.; Bhaskar, A.; Li, J.; Passerini, S.; Winter, M. Cu$_3$P Binary Phosphide: Synthesis via a Wet Mechanochemical Method and Electrochemical Behavior as Negative Electrode Material for Lithium-Ion Batteries. *Adv. Energy Mater.* **2013**, *3*, 231–238.

(15) Poli, F.; Wong, A.; Kshetrimayum, J. S.; Monconduit, L.; Letellier, M. In Situ NMR Insights into Electrochemical Reaction of Cu$_3$P Electrodes in Lithium Batteries. *Chem. Mater.* **2016**, *28*, 1787–1793.

(16) Liu, S.; Liu, C.; Guo, J.; Yan, W. Microstructure and Superior Electrochemical Activity of Cu$_3$P/Reduced Graphene Oxide Composite for an Anode in Lithium-Ion Batteries. *J. Electrochem. Soc.* **2017**, *164*, A2390–A2397.

(17) Chen, Y.-C.; Chen, Z.-B.; Lin, Y.-G.; Hsu, Y.-K. Synthesis of Copper Phosphide Nanotube Arrays as Electrodes for Asymmetric Supercapacitors. *ACS Sustainable Chem. Eng.* **2017**, *5*, 3863–3870.

(18) Liu, S., He, X.; Zhu, J.; Xu, L.; Tong, J. Cu$_3$P/RGO Nanocomposite as a New Anode for Lithium-Ion Batteries. *Sci. Rep.* **2016**, *6*, 35189.

(19) Shi, Y.; Zhang, B. Recent advances in transition metal phosphide nanomaterials: synthesis and application in hydrogen evolution reaction. *Chem. Soc. Rev.* **2016**, *45*, 1529–1541.

(20) Bai, Y.; Fang, L.; Xu, H.; Gu, X.; Zhang, H.; Wang, Y. Strengthened Synergistic Effect of Metallic M$_x$P$_y$ (M = Co, Ni, and Cu) and Carbon Layer via Peapod-Like Architecture for Both Hydrogen and Oxygen Evolution Reactions. *Small* **2017**, *13*, 1603718–1603718.

(21) Du, H.; Zhang, X.; Tan, Q.; Kong, R.; Qu, F. A Cu$_3$P–CoP hybrid nanowire array: a superior electrocatalyst for acidic hydrogen evolution reactions. *Chem. Commun.* **2017**, *53*, 12012–12015.

(22) Han, A.; Zhang, H.; Yuan, R.; Ji, H.; Du, P. Crystalline Copper Phosphide Nanosheets as an Efficient Janus Catalyst for Overall Water Splitting. *ACS Appl. Mater. Interfaces* **2017**, *9*, 2240–2248.

(23) Lu, C.; Wang, J.; Czioska, S.; Dong, H.; Chen, Z. Hierarchically Structured Cu-Based Electrocatalysts with Nanowires Array for Water Splitting. *J. Phys. Chem. C* **2017**, *121*, 25875–25881.

(24) Yue, X.; Yi, S.; Wang, R.; Zhang, Z.; Qiu, S. A novel and highly efficient earth-abundant Cu$_3$P with TiO2 "P–N" heterojunction nanophotocatalyst for hydrogen evolution from water. *Nanoscale* **2016**, *8*, 17516–17523.

(25) Read, C. G.; Callejas, J. F.; Holder, C. F.; Schaak, R. E. General Strategy for the Synthesis of Transition Metal Phosphide Films for Electrocatalytic Hydrogen and Oxygen Evolution. *ACS Appl. Mater. Interfaces* **2016**, *8*, 12798–12803.

(26) Wei, S.; Qi, K.; Jin, Z.; Cao, J.; Zheng, W.; Chen, H.; Cui, X. One-Step Synthesis of a Self-Supported Copper Phosphide Nanobush for Overall Water Splitting. *ACS Omega* **2016**, *1*, 1367–1373,

(27) Hou, C.-C.; Chen, Q.-Q.; Wang, C.-J.; Liang, F.; Lin, Z.; Fu, W. F.; Chen, Y. Self-Supported Cedarlike Semimetallic Cu$_3$P Nanoarrays as a 3D High-Performance Janus Electrode for Both Oxygen and Hydrogen Evolution under Basic Conditions. *ACS Appl. Mater. Interfaces* **2016**, *8*, 23037–23048.

(28) Ma, L.; Shen, X.; Zhou, H.; Zhu, J.; Xi, C.; Ji, Z.; Kong, L. Synthesis of Cu$_3$P nanocubes and their excellent electrocatalytic efficiency for the hydrogen evolution reaction in acidic solution. *RSC Adv.* **2016**, *6*, 9672–9677.

(29) Tian, J.; Liu, Q.; Cheng, N.; Asiri, A. M.; Sun, X. Self-Supported Cu$_3$P Nanowire Arrays as an Integrated High-Performance Three-Dimensional Cathode for Generating Hydrogen from Water. *Angew. Chem. Int. Ed.* **2014**, *53*, 9577–9581.

(30) Feng, L.; Xue, H. Advances of transition metal phosphide application in electrochemical energy storage and catalysis. *ChemElectroChem* **2017**, *4*, 20–34.

(31) Callejas, J. F.; Read, C. G.; Roske, C. W.; Lewis, N. S.; Schaak, R. E. Synthesis, Characterization, and Properties of Metal Phosphide Catalysts for the Hydrogen-Evolution Reaction. *Chem. Mater.* **2016**, *28*, 6017–6044.

(32) Xiao, P.; Chen, W.; Wang, X. A Review of Phosphide-Based Materials for Electrocatalytic Hydrogen Evolution *Adv. Energy Mater.* **2015**, *5*, 1500985.

(33) Schlenger, H.; Jacobs, H.; Juza, R. Ternäre Phasen des Lithiums mit Kupfer und Phosphor. *Z. Anorg. Allg. Chem.* **1971**, *385*, 177–201.

(34) De Trizio, L.; Gaspari, R.; Bertoni, G.; Kriegel, I.; Moretti, L.; Scotognella, F.; Maserati, L.; Zhang, Y.; Messina, G. C.; Prato, M.; Marras, S.; Cavalli, A.; Manna, L. Cu$_{3-x}$P Nanocrystals as a Material Platform for Near-Infrared Plasmonics and Cation Exchange Reactions. *Chem. Mater.* **2015**, *27*, 1120–1128.

(35) Wolff, A.; Pallmann, J.; Boucher, R.; Weiz, A.; Brunner, E.; Doert, T.; Ruck, M. Resource-Efficient High Yield Ionothermal Synthesis of Microcrystalline Cu$_{3-x}$P. *Inorg. Chem.* **2016**, *55*, 8844–8851.

(36) Manna, G.; Bose, R.; Pradhan, N. Semiconducting and Plasmonic Copper Phosphide Platelets. *Angew. Chem. Int. Ed.* **2013**, 52, 6762–6766.

(37) Sun, T.; Wang, Y.; Yu, W.; Wang, Y.; Dai, Z.; Liu, Z.; Shivananju, B. N.; Zhang, Y.; Fu, K.; Shabbir, B.; Ma, W.; Li, S.; Bao, Q. Flexible Broadband Graphene Photodetectors Enhanced by Plasmonic Cu$_{3-x}$P Colloidal Nanocrystals. *Small* **2017**, *13*, 1701881.

(38) Lê Anh, M.; Wolff, A.; Kaiser, M. ; Yogendra, S.; Weigand, J. J.; Pallmann, J.; Brunner, E. ; Ruck, M.; Doert, T. Mechanistic exploration of the copper(I) phosphide synthesis in phosphonium-based and phosphorus-free ionic liquids. *Dalton Trans.* **2017**, *46*, 15004–15011.

(39) Brauer, G. Handbuch der Präparativen Anorganischen Chemie, 3rd ed.; F. Enke: Stuttgart, 1962.

(40) Petříček, V.; Dušek, M.; Palatinus, L. Crystallographic Computing System JANA2006: General features. *Z. Kristallogr.-Cryst. Mater.* **2014**, *229*, 345–352.

(41) Petříček, V.; Dušek, M.; Palatinus, L. Jana2006, The Crystallographic Computing System Version 25/10/2015, Institut of Physics, Academy of Sciences of the Czech Republik, Prague, 2015.

(42) Oszlányi, G.; Sütő, A. The charge flipping algorithm. *Acta Crystallogr., Sect. A: Found. Crystallogr.* **2008**, *64*, 123–134.

(43) Oszlányi, G.; Sütő, A. Ab initio structure solution by charge flipping. *Acta Crystallogr., Sect. A: Found. Crystallogr.* **2004**, *60*, 134–141.

(44) Brandenburg, K. Diamond 3.2k - Crystal and Molecular Structure Visualization, Crystal Impact GbR, Bonn, 2014.

(45) Furó, I.; Bakonyi, I.; Tompa, K.; Zsoldos, É.; Heinmaa, I.; Alla, M.; Lippmaa, E. Nuclear Magnetic Resonance Knight Shift and Linewidth in Ni_3P and Cu_3P : A Magic-Angle Spinning Study. *J. Phys. Condens. Matter* **1990**, *2*, 4217–4225.

(46) Mauvernay, B.; Doublet, M.-L.; Monconduit, L. Redox mechanism in the binary transition metal phosphide Cu_3P. *J. Phys. Chem. Solids* **2006**, *67*, 1252.

(47) Jones, R. O.; Hohl, D. Structure of phosphorus clusters using simulated annealing–P_2 to P_8. *J. Chem. Phys.* **1990**, *92*, 6710–6721.

(48) Schoeller, W. W.; Staemmler, V.; Rademacher, P.; Niecke, E. Theoretical studies on inorganic ring systems. Tetraphosphabicyclobutane, cyclotriphosphane, and white phosphorus: ring strain and hybridization. *Inorg. Chem.* **1986**, *25*, 4382–4385.

(49) Scheer, M.; Balázs, G.; Seitz, A. P_4 Activation by Main Group Elements and Compounds. *Chem. Rev.* **2010**, *110*, 4236–4256.

(50) Holthausen, M. H.; Weigand, J. J. The chemistry of cationic polyphosphorus cages – syntheses, structure and reactivity. *Chem. Soc. Rev.* **2014**, *43*, 6639–6657.

(51) Perry, D. L. *Handbook of Inorganic Compounds*; CRC Press: Boca Raton, 1995; p. 293.

(52) Boros, È.; Earle, M. J; Gîlea, M. A.; Metlen, A.; Mudring, A.-V.; Rieger, F.; Robertson, A. J.; Seddon, K. R.; Tomaszowska, A. A.; Trusov, L.; Vyle, J. S. On the dissolution of non-metallic solid elements (sulfur, selenium, tellurium and phosphorus) in ionic liquids. *Chem. Commun.* **2010**, *46*, 716–718.

(53) Groh, M. F.; Paasch, S.; Weiz, A.; Ruck, M.; Brunner, E. Unexpected Reactivity of Red Phosphorus in Ionic Liquids. *Eur. J. Inorg. Chem.* **2015**, 3991–3994.

(54) Olofsson, O. The Crystal Structures of CuP_2 and AgP_2 with some Phase Analytical Data of the Cu-P and Ag-P Systems. *Acta Chem. Scand.* **1965**, *19*, 229–241.

(55) Möller, M. H.; Jeitschko, W. Darstellung, Eigenschaften und Kristallstruktur von Cu_2P_7 und Strukturverfeinerungen von CuP_2 und AgP_2. *Z. Anorg. Allg. Chem.* **1982**, *491*, 225–236.

(56) Lange, S.; Bawohl, M.; Weihrich, R.; Nilges, T. Mineralization Routes to Polyphosphides: Cu_2P_{20} and Cu5InP16. *Angew. Chem. Int. Ed.* **2008**, *47*, 5654–5657.

(57) Santner, S.; Yogendra, S.; Weigand, J. J.; Dehnen, S. Exploring the Chemical ReactionSpace at the Formation of Chalcogenidometalate Superspheres in Ionic Liquids. *Chem. Eur. J.* **2017**, *23*, 1999–2004.

(58) Dragulescu-Andrasi, A.; Miller, L. Z.; Chen, B,; McQuade, D. T.; Shatruk, M. Facile Conversion of Red Phosphorus into Soluble Polyphosphide Anions by Reaction with Potassium Ethoxide. *Angew. Chem. Int. Ed.* **2016**, 55, 3904–3908.

(59) Pietro Oliveri, I.; Di Bella, S. Lewis basicity of relevant monoanions in a non-protogenic organic solvent using a zinc(II) Schiff-base complex as a reference Lewis acid. *Dalton Trans.* **2017**, *46*, 11608–11614.

(60) Schmeisser, M.; van Eldik, R. Elucidation of inorganic reaction mechanisms in ionic liquids: the important role of solvent donor and acceptor properties. *Dalton Trans.* **2014**, *43*, 15675–15692.

(61) Holzweber, M.; Lungwitz, R.; Doerfler, D.; Spange, S.; Koel, M.; Hutter, H.; Linert, W. Mutual Lewis Acid–Base Interactions of Cations and Anions in Ionic Liquids. *Chem. Eur. J.* **2013**, *19*, 288–293.

(62) Schmeisser, M.; Illner, P.; Puchta, R.; Zahl, A.; van Eldik, R. Gutmann Donor and Acceptor Numbers for Ionic Liquids. *Chem. Eur. J.* **2012**, *18*, 10969–10982.

(63) Wang, B.; Qin, L.; Mu, T.; Xue, Z.; Gao, G. Are Ionic Liquids Chemically Stable? *Chem. Rev.* **2017**, *117*, 7113–7131.

(64) Juza, R.; Bär, K. Leiter und Halbleiter unter den Phosphiden der ersten und zweiten Nebengruppe. *Z. Anorg. Allg. Chem.* **1956**, *283*, 230–245.

(65) Kochelaev, B. I. Spin-Phonon Interaction and the EPR Linewidth in La_2CuO_4 and Related Cuprates *J. Supercond.* **1999**, *12*, 53–55.

(66) Flinn, P. A.; McManus, G. M.; Rayne, J. A. Elastic constants of ordered and disordered Cu_3Au from 4.2 to 300°K *J. Phys. Chem. Solids* **1960**, *15*, 189–195.

(67) Bärnighausen, H. Group-subgroup relationships between space groups: A useful tool in crystal chemistry. *MATCH Commun. Math. Comput. Chem.* **1980**, *9*, 139–175.

(68) Wondratschek, H.; Müller, U. (Eds.), *International Tables for Crystallography*; International Union of Crystallography: Chester, 2011.

(69) Kroumova, E.; M. Perez-Mato, J.; Aroyo, M. I. WYCKSPLIT: a computer program for determination of the relations of Wyckoff positions for a group-subgroup pair. *J. Appl. Crystallogr.* **1998**, *31*, 646.

(70) Stokes, H. T.; Campbell, B. J.; van Smaalen, S. Generation of (3+ *d*)-dimensional superspace groups for describing the symmetry of modulated crystalline structures. *Acta Crystallogr., Sect. A: Found. Crystallogr.* **2011**, *67*, 45–55.

(71) Mauvernay, B.; Bichat, M.-P.; Favier, F. ; Monconduit, L. Morcrette, M.; Doublet, M.-L. Progress in the Lithium Insertion Mechanism in Cu_3P. *Ionics* **2005**, *11*, 36–45.

(72) Bichat, M.-P.; Politova, T.; Pascal, J. L.; Favier, F.; Monconduit, L. Electrochemical Reactivity of Cu3P with Lithium. *J. Electrochem. Soc.* **2004**, *151*, A2074–A2081.

(73) Crosnier, O.; Nazar, L. F. Facile Reversible Displacement Reaction of Cu3P with Lithium at Low Potential. *Electrochem. Solid-State Lett.* **2004**, *7*, A187–A189.

(74) Crosnier, O.; Mounsey, C.; Herle, P. S.; Taylor, N.; Nazar, L. F. Crystal Structure and Electrochemical Behavior of Li_2CuP: a Surprising Reversible Crystalline-Amorphous Transformation *Chem. Mater.* **2003**, *15*, 4890–4892.

(75) Dong, Y.; DiSalvo, F. J. Reinvestigation of trilithium phosphide, Li_3P. *Acta Crystallogr., Sect. E: Struct. Rep. Online* **2007**, *63*, i97–i98.

(76) Nazri, G. Preparation, structure and ionic conductivity of lithium phosphide. *Solid State Ionics* **1989**, *34*, 97–102.

Insert Table of Contents artwork here